Aeropropulsive Assessment of a BLI Tail-Cone Thruster Propulsion System for the NASA Common Research Model and a Transonic Truss-Braced Wing Configuration

Leonardo Machado*, and Timothy Chau†
Science & Technology Corporation, Moffett Field, California, 94035

Jared C. Duensing‡
NASA Ames Research Center, Moffett Field, California, 94035

This paper presents an investigation into the potential benefits of a boundary layer ingestion (BLI) aft fuselage propulsion system, or tail-cone thruster (TCT), when applied to two transport category aircraft: a conventional tube-and-wing configuration based on the NASA Common Research Model (CRM) and a transonic truss-braced wing (TTBW) configuration. Through the ingestion of low-momentum flow developed over the airframe of an aircraft, the TCT propulsion system technology can reduce overall power consumption and hence fuel burn and emissions. However, an accurate assessment of this potential requires the application of high-fidelity analysis tools that can capture the relevant propulsion-airframe integration effects, at least to first order. Toward this end, the present study employs aeropropulsive analysis tools based on the Reynolds-averaged Navier-Stokes equations to estimate the power savings coefficient, measured relative to equivalent non-BLI configurations of a given airframe. Results indicate shaft power savings of 4.1% and 5.9% can be obtained for the boundary-layer ingesting TCT configuration of the CRM and TTBW, respectively. The present study also examines the coupling between airframe aerodynamics and the inlet flow distortion experienced by the TCT of a given aircraft configuration through airframe component sensitivity studies.

Nomenclature

α	=	Angle of attack
γ	=	Specific heat ratio of air
η_{a}	=	Adiabatic efficiency
η_{trans}	=	Transmission efficiency
C_L	=	Lift coefficient
C_D	=	Drag coefficient
c_p	=	Specific heat capacity of air
h	=	Specific enthalpy
M	=	Mach number
$\dot{m}$	=	Mass flow rate
P	=	Shaft power
p	=	Pressure
Re	=	Reynolds number
R	=	Gas constant of air
T	=	Temperature

*Research Scientist/Engineer, Computational Aerosciences Branch, NAS Division, AIAA Member, leonardo.machado@nasa.gov
†Senior Research Scientist/Engineer, Computational Aerosciences Branch, NAS Division, AIAA Member, timothy.chau@nasa.gov
‡Computational Aerosciences Branch Chief, Computational Aerosciences Branch, NAS Division, AIAA Member, jared.c.duensing@nasa.gov

Acronyms

BLI	=	Boundary Layer Ingestion
CFD	=	Computational Fluid Dynamics
EAP	=	Electrified Aircraft Propulsion
FPR	=	Fan Pressure Ratio
LAVA	=	Launch, Ascent, and Vehicle Aerodynamics
NTF	=	National Transonic Facility
PR	=	Pressure Recovery
PSC	=	Power Savings Coefficient
PAI	=	Propulsion-Airframe Integration
RANS	=	Reynolds-Averaged Navier Stokes
TCT	=	Tail-Cone Thruster

I. Introduction

Driven by the aviation industry's increasing focus on environmental sustainability, advanced aircraft technologies are being sought to enhance fuel efficiency, reduce emissions, and more generally, improve the overall energy efficiency of the sector. Within this context, boundary layer ingestion (BLI) is a technology that offers improved propulsive efficiency through the ingestion of low-momentum boundary layer flow from the airframe. This is achieved by embedding a given propulsor into the airframe, reducing engine inlet and exit flow velocities, diminishing ram drag, and decreasing nacelle and pylon wetted area and weight [1]. Although the concept was first introduced by Smith and Roberts [2] in 1947 for aircraft applications, the technology was not extensively pursued then. More recently, however, there has been a renewed interest in BLI for transport category aircraft, with several new aircraft concepts leveraging the technology. These include the D8 [3] and hybrid-/blended-wing body aircraft [4–6]. The resurgence has also been in part motivated by advancements in electrified aircraft propulsion (EAP) technology, which has expanded the propulsion system design space, for example in terms of the number and positioning of electric propulsors. Example turbo- and hybrid-electric aircraft leveraging BLI technology include NASA's STARC-ABL [7], N3X [8], and SUSAN Electrofan concepts [9, 10], and the ONERA DRAGON [11].

However, assessing the benefits of BLI technology still remains a challenge given the coupling between aerodynamics and propulsion, and the impact of the boundary layer flow on turbomachinery performance. Assessments of the technology also depend on the type of BLI technology being pursued, which can involve distinct flow physics. Specifically, Type I BLI, or 180-degree distortion, involves the ingestion over the bottom portion of the engine inlet of boundary layer flow typically developed on the top of a wing or fuselage, for example the D8 [3]. Type II BLI, or 360-degree distortion, involves the ingestion of a radially stratified boundary layer typically developed around a fuselage [12], e.g. the STARC-ABL [7].

Nonetheless, high-fidelity aeropropulsive simulation tools for design and analysis have proven invaluable for understanding the first-order effects governing the coupling of the two disciplines; see for example [13–18]. Rodriguez [13] conducted a design of BLI inlets for a blended wing body aircraft concept utilizing a coupled design tool consisting of a RANS flow solver, an engine analysis method, and a nonlinear optimizer. This study highlighted the strong coupling between the airframe aerodynamics and the propulsion system, and found that the BLI configuration offered reductions in airframe drag compared to a podded alternative. Further studies from Gray et al. [14] also utilized a coupled propulsion-aerodynamic for the analysis of a BLI propulsion system using a 1D cycle propulsion model and a RANS aerodynamic model. Findings from this research indicated that the BLI configuration provided benefits to both the propulsion and aerodynamic systems relative to a conventional podded configuration. For the propulsion system, the main benefit stemmed from a lower incoming momentum flux, whereas for the aerodynamics, the main contributor was an increase in static pressure along the aft section of the fuselage caused by the influence of the BLI fan. Finally, Yildirim et al. [18], using a CFD-based aeropropulsive design framework to optimize the STARC-ABL concept, found that BLI designs with smaller fans and higher FPR presented higher shaft power savings. The analyses showed that as the BLI fan size increases, it begins to ingest flow beyond the boundary layer, thereby diminishing the benefits of BLI.

Overall, these research efforts emphasized the importance of employing computational fluid dynamics (CFD) tools in 3D to accurately predict the airflow over the airframe and to capture its impact on the propulsion systems, and the impact of the thrust-producing propulsion systems on the aerodynamics of the airframe through actuator disk and zone methods.

Shaft power savings of up to 4.6% could be achieved, depending on the configuration and electrical transmission efficiency assumed, with more aggressive applications of BLI having the potential to achieve savings of up to 10% [15].

Despite these potential benefits, BLI also comes with the challenge of inlet flow distortion, namely, spatial non-uniformities in the velocity and pressure field [19], which introduce performance penalties and design complexity on fans operating under these conditions. As emphasized by Gray et al. [17], distortion penalties have the potential to undermine BLI benefits or, in more severe cases, lead to structural failure of turbomachinery components.

Recent investigations have examined the impact of inlet distortion, utilizing both computational methods [20, 21] and wind-tunnel tests [22–25]. Kenway and Kiris [21] conducted studies that successfully minimized inlet distortion for the aft-mounted BLI propulsor of the STARC-ABL through the application of aeropropulsive shape optimization. This work identified the main contributors to distortion at the propulsor fan face as the non-axisymmetric fuselage and wing downwash. Furthermore, work by Gray et al. [17] studied the impact of a distortion constraint on the performance of three different BLI propulsor sizes for the STARC-ABL configuration. Results showed that satisfying the distortion constraint negatively affects propulsion system efficiency, highlighting a tradeoff between overall propulsion system efficiency and the adiabatic efficiency and structural loading of the fan.

In the present paper, high-fidelity aeropropulsive CFD analysis tools are used to investigate the potential benefits of a Type II BLI propulsion system in the form of a tail-cone thruster (TCT) when applied to a wide-body conventional tube-and-wing aircraft based on the NASA Common Research Model (CRM) [26] and a single-aisle transonic truss-braced wing (TTBW). More specifically, the former is based on a 2.7%-scale model of the CRM retrofitted with an aft fuselage propulsor, which is being used at NASA to study BLI and propulsion-airframe integration (PAI) via computational tools and wind tunnel tests [27–29]. The latter is a NASA-developed geometry used to study the design and performance of the truss-braced wing configuration at Mach 0.80, an unconventional aircraft configuration featuring a large span wing supported by a structurally efficient strut-brace system, which has the potential to significantly reduce aviation fuel burn.

Performance is measured based on the power savings coefficient (PSC) metric [30] as done in [15–18]. Specifically, for each aircraft configuration, comparisons of shaft power are made between a BLI configuration, which consists of two underwing turbofans and an aft-mounted BLI electric propulsor, and a conventional or non-BLI configuration featuring two underwing turbofans.

The present paper also aims to provide insights into the main contributions to the inlet distortion profile of each airframe, which is particularly of interest for the TTBW given its unconventional nature. This is achieved through a component-based sensitivity study where airframe components are systematically added to the grid system in an aircraft system buildup followed by CFD simulations for observing the resulting flow distortion patterns.

The paper is structured as follows. Section II details the approach employed for the PSC assessment. Section III provides information on the two aircraft models studied. In Section IV, the computational methods and tools used in this work are introduced. The results of the PSC study are presented in Section V, while Section VI examines the inlet flow distortion patterns of the aircraft under investigation. Lastly, Section VII provides a summary of the main findings and discusses their implications. Future work is also addressed.

II. Approach to Estimating the Power Savings Coefficient

Previous research [30–32] highlighted the limitations of traditional thrust-drag-based accounting methods in coupled aeropropulsive problems. As an alternative, Smith [30] introduced PSC as a power-based metric for evaluating the performance of BLI propulsion systems. PSC measures the relative difference in the propulsive power required by a BLI configuration, P_{BLI}, compared to a non-BLI configuration, $P_{\text{non-BLI}}$, and is given by

$$\text{PSC} = \frac{P_{\text{non-BLI}} - P_{\text{BLI}}}{P_{\text{non-BLI}}} \tag{1}$$

Here, $P_{\text{non-BLI}}$ is the power required by a conventional twin-engine aircraft configuration, which serves as a reference point. Furthermore, the present work follows the approach of Gray et al. [15, 17], which focuses on shaft power and assumes a turbo- or hybrid-electric propulsion system for the BLI configuration. Specifically, power requirements are determined as follows:

$$P_{\text{non-BLI}} = 2P_{\text{pod}} \tag{2}$$

$$P_{\text{BLI}} = \frac{P_{\text{TCT}}}{\eta_{\text{trans}}} + 2P_{\text{pod}} \tag{3}$$

where P_{pod} and P_{TCT} are the shaft power of the podded propulsors and TCT, respectively, and η_{trans} is the transmission efficiency, assumed to be a constant value of 90% based on prior studies at NASA [7], and represents a powertrain end-to-end transmission efficiency based on nominal EAP technology level projections.

In order to obtain estimates of the shaft power required by the conventional configuration, CFD simulations are first performed to compute total drag for a given set of gross thrust inputs to the two underwing turbofans, assuming an equal distribution of thrust, or thrust split, across the two propulsors. These turbofans are modeled as "free-air" podded propulsors that consist of a hub and nacelle following Gray et al. [15, 17]. The thrust inputs are then iterated to achieve a net streamwise force of zero. This yields the design point shaft power. For the BLI configuration, the same approach is followed except with a thrust split of 1/3 and 2/3 between the TCT and the two podded propulsors.

Once the trim condition has been determined, the shaft power required by the fan to compress the flow can be approximated as:

$$P = \dot{m}\Delta h \tag{4}$$

where $\dot{m}$ is the mass flow rate of each propulsion unit and Δh is the specific enthalpy change across a given fan. Specific enthalpy is calculated from

$$\Delta h = c_p(T_{t_3} - T_{t_0}) = \frac{1}{\eta_a}\left(\frac{\gamma R}{\gamma - 1}\right) T_{t_0}\left(\text{FPR}^{\frac{\gamma-1}{\gamma}} - 1\right) \tag{5}$$

where c_p, γ, and R are the specific heat capacity, specific heat ratio, and gas constant of air, respectively. T_{t_0} is the total temperature at the start of the fan face, T_{t_3} is the total temperature at the fan exit, and FPR is the fan pressure ratio. The adiabatic efficiency is calculated based on the method of Gray et al. [33], which is based on a linear regression of data published in two studies on next-generation subsonic transport aircraft under the NASA Advanced Air Transport Technologies Project [34, 35]:

$$\eta_a = 1.066 - 0.0866\ \text{FPR} \tag{6}$$

It should be noted that in addition to the simplifying assumptions described above, several other assumptions are made in the current work. For example, the fan stage adiabatic efficiency does not account for inlet distortion penalties introduced by BLI, including associated losses. Drag penalties related to the integration of the podded propulsors are also excluded, such as drag contributions from pylons, and wing and pylon interference. Lastly, all simulations are performed at a fixed angle of attack, corresponding to the airframe's constant lift trim condition. This assumes that the propulsion system's contributions to lift are negligible. It should also be noted that although a constant thrust split is assumed for the BLI configuration, the thrust split should be recognized as a key design parameter in future work given its influence on the sizing of the BLI propulsor and hence the relative impact of inlet flow distortion, as highlighted by Gray et al. [17] and Yildirim et al. [18].

III. Aircraft Configurations

The present paper considers the application of the TCT technology to two aircraft configurations: a wide-body conventional tube-and-wing based on the NASA CRM [26], and a single-aisle TTBW. The first establishes the approach based on a well-studied conventional aircraft configuration, while the second assesses whether benefits can also be obtained when implemented on a high wing span aircraft with a high-wing configuration and a truss topology.

For the conventional tube-and-wing configuration, a variant of the NASA CRM is used, shown in Fig. 1a. The NASA CRM is a transport aircraft similar to the Boeing 777, with a cruise Mach number and lift coefficient, C_L, of 0.85 and 0.50, respectively, and a cruise Reynolds number of 40 million [26]. The NASA CRM is an open geometry that has undergone comprehensive testing in various wind tunnels, making it a widely used model for CFD code validation (see for example [36–38]). The specific variant used in this study is a CRM model retrofitted with a BLI TCT [27], as shown in Fig. 1c. This aircraft configuration is herein referred to as the CRM-TCT. A 2.7% scale model of this configuration was subject to wind tunnel testing at the National Transonic Facility (NTF) and is part of ongoing research efforts supporting the validation of CFD solvers for BLI and PAI assessments [27–29]. For the CRM-TCT, the design Mach number and lift coefficient of the CRM are used, with the remaining flow conditions adjusted to achieve a Reynolds number of 40 million.

With regard to the TTBW configuration, a NASA-developed aircraft geometry is used, shown in Fig. 1b. This aircraft concept, referred to in the present study as the TTBW, is a single-aisle aircraft designed for Mach 0.80 with a lift coefficient of 0.60 and a Reynolds number of 13.02 million. This aircraft geometry was developed through the methods presented in Chau and Zingg [39, 40] and is based on the conceptual design studies found in Bradley et al. [41]. The TTBW has a 170 ft wing span supported by a main strut, which improves aerodynamic efficiency while reducing wing

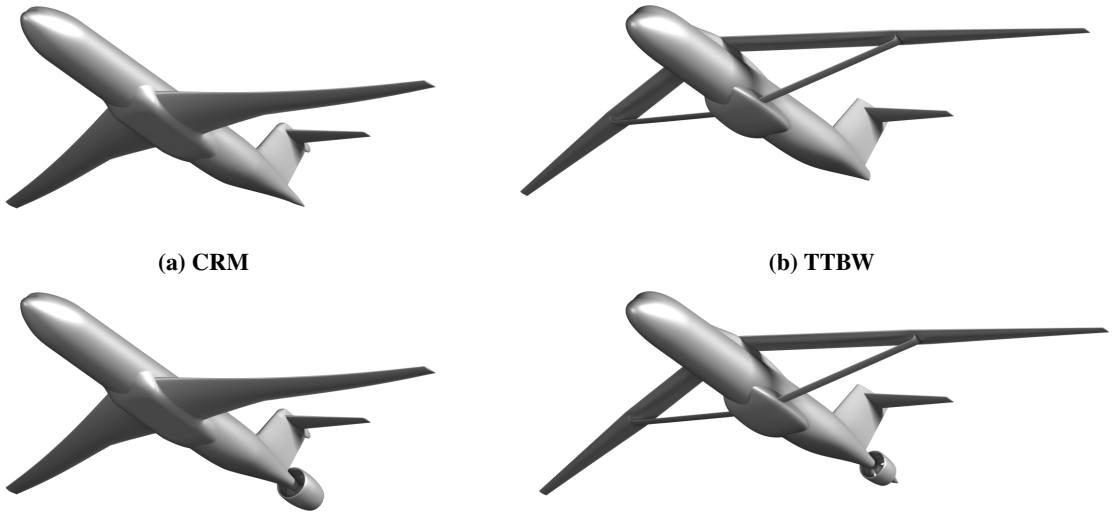

(a) CRM **(b) TTBW**

(c) CRM-TCT **(d) TTBW-TCT**

Fig. 1 Aircraft configurations modified to include BLI TCT propulsion systems.

weight penalties. As with the CRM-TCT, a TCT is attached to the aft fuselage of the TTBW, as shown in Fig. 1d, and the wing system is positioned further aft to accommodate tail strike considerations to first order. This increases the influence of the truss-braced wing system on the flow experienced by the TCT. This aircraft configuration is herein referred to as the TTBW-TCT.

Accompanying these airframe geometries are models of the podded propulsors, simulated in "free air" as describe in Section II. These propulsors represent the underwing turbofans of the BLI and non-BLI configurations and are simplified to consist of only a hub and nacelle. Although this excludes the core flow and other gas turbine cycle considerations, this simplification allows for a focus on first-order aeropropulsive interactions. These podded propulsors are based on the TCT geometry but resized based on their thrust requirements, assuming maximum thrust correlates with nacelle capture area. For simulating thrust, the fan of a given propulsor is modeled as an axisymmetric actuator zone. Additional details on the actuator zone method are provided in Section IV. Figs. 2 and 3 show the computational models of the CRM and CRM-TCT, and the TTBW and TTBW-TCT, respectively, which include the free-flying propulsors and highlight the actuator zones of each propulsion system.

Table 1 provides the operating conditions considered for each aircraft configuration. Note that for the assessments of BLI versus non-BLI, the configurations of a given aircraft concept are simulated at the same conditions for direct comparisons. These operating points correspond to the nominal cruise conditions of each aircraft concept.

Table 1 Aircraft configuration characteristics and operating conditions.

Parameter	CRM	TTBW
Mean aerodynamic chord (ft)	22.98	9.17
Reference area (ft^2)	4,130	1,467
Mach number	0.85	0.80
Altitude (ft)	38,530	41,500
Reynolds number (10^6)	40.00	13.02
Lift coefficient	0.50	0.60

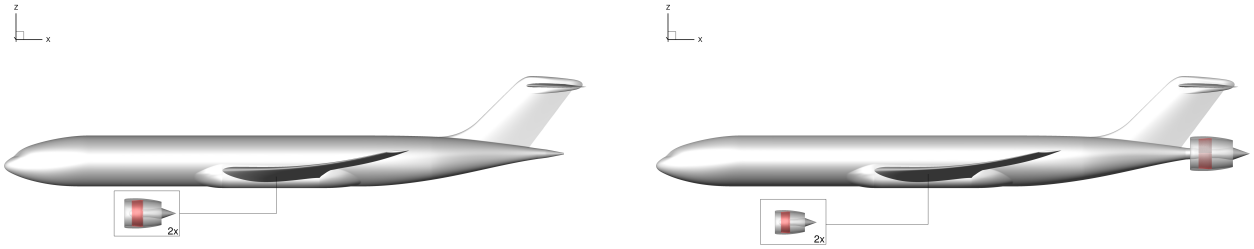

(a) CRM (b) CRM-TCT

Fig. 2 Computational models of the CRM and CRM-TCT, with actuator zones shown in red. Free-flying podded propulsors are included separately to model the underwing propulsion systems.

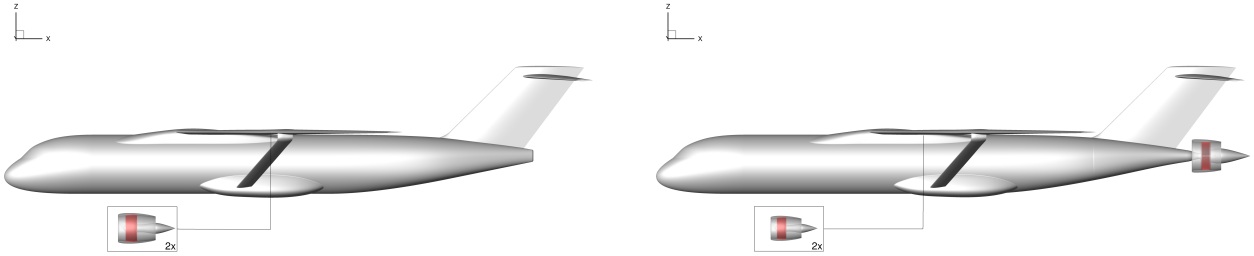

(a) TTBW (b) TTBW-TCT

Fig. 3 Computational models of the TTBW and TTBW-TCT, with actuator zones shown in red. Free-flying podded propulsors are included separately to model the underwing propulsion systems.

IV. Computational Methodology

For performing high-fidelity aeropropulsive analysis, the present study uses the structured curvilinear overset solver within the Launch, Ascent, and Vehicle Aerodynamics (LAVA) framework [42]. Specifically, this work considers the steady-state compressible Reynolds-averaged Navier-Stokes (RANS) equations in strong conservation law form, and employs a second-order discretization. Convective fluxes are computed using a modified Roe scheme with third-order upwind-biased flux reconstruction and the Koren flux limiter [43, 44]. Viscous fluxes are discretized using a mid-point and node-centered difference scheme. The turbulence closure model chosen is the one-equation Spalart-Allmaras (SA) turbulence model [45] with Rotation Curvature [46] and Quadratic Constitutive Relationship corrections [47] (SA-RC-QCR2000).

The discretized set of non-linear equations is marched in pseudo-time to steady-state using automatic CFL ramping to accelerate convergence. At each pseudo-time step, the linear system is solved using the preconditioned generalized minimal residual (GMRES) algorithm [48]. The preconditioner is obtained from an incomplete lower-upper factorization with fill level 0 of a first-order approximation of the residual Jacobian.

For modeling propulsion, an actuator zone method is used, as presented in [49]. In this method, the thrust produced by the fans is modeled with an axisymmetric volume of fluid where source terms contribute to a constant radial thrust distribution. Torque effects are neglected and the pressure rise is isentropic. Since low FPRs are considered in this work, the absence of a temperature rise does not significantly affect the resulting flowfield. However, since fan efficiency plays an important role in estimating the performance of the propulsion system, it is accounted for when calculating fan shaft power as described in Section II.

For all computational grids, mesh resolution is based on the gridding guidelines of the 6th AIAA Drag Prediction Workshop [50] and grid refinement studies presented in [28].

V. High-Fidelity Aeropropulsive Assessments via the Power Savings Coefficient

This section presents assessments of the TCT technology applied to the CRM and TTBW configurations through the application of high-fidelity aeropropulsive analysis. This includes results from the thrust sweep studies used to

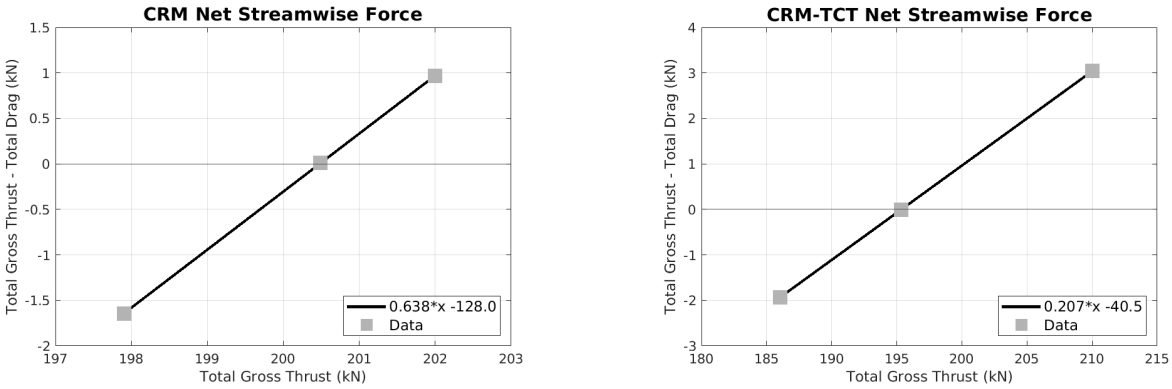

(a) CRM **(b) CRM-TCT**

Fig. 4 Net streamwise force versus total gross thrust input for the CRM and CRM-TCT configurations.

determine the trim condition of each aircraft geometry, performance assessments at these trim conditions, and lastly calculations of PSC for each of the aircraft configurations.

A. The NASA Common Research Model

In order to estimate PSC for the CRM-TCT configuration, the airframes of the CRM and CRM-TCT are first trimmed with respect to angle of attack, α, to satisfy their cruise lift coefficients. For a design C_L of 0.50, the CRM and CRM-TCT are trimmed at $\alpha = 2.12°$ and $\alpha = 2.11°$, respectively. These are obtained with the models of the free-air propulsors omitted and all propulsion systems turned off, assuming their contributions to lift are negligible for the purposes of this study.

The CRM and CRM-TCT are next trimmed with respect to gross thrust input to achieve a net zero streamwise force. This is shown in Figure 4 where steady-state flow simulations are performed iteratively with gross thrust input to determine the thrust-drag trim condition via linear interpolation. Recall that the thrust split determines the thrust share of each propulsion unit and that the gross thrust input of a given propulsor corresponds to the thrust distributed uniformly across the actuator zone volume nodes. For the CRM, a gross thrust input of 100.2 kN is required from each wing propulsor to balance drag, while for the CRM-TCT, a gross thrust of 65.1 kN is needed from each wing propulsor and the TCT.

Table 2 provides the drag coefficient, C_D, of the wing propulsors and airframe, with the latter including the TCT for the CRM-TCT at the trim condition. Due to the differences in thrust share between the wing propulsors of the CRM (50:50) and those of the CRM-TCT (33:33), the drag of the former set is much higher as a result of higher thrust-induced drag. This difference is also due to the difference in propulsor sizing. A sense for this is given by the flow-through data, which includes the drag of the airframe, wing propulsors, and TCT at a power setting of zero. Here, the CRM's wing propulsors experience 12.2 counts less drag than those of the CRM-TCT. It is also worth noting that the addition of the TCT results in a 15.6 counts increase in the airframe drag of the CRM-TCT compared to the CRM for the same lift coefficient. The flow-through cases also provide a reference point for the magnitude of the thrust-induced drag contributions from the power-on cases, which would normally be hidden within the net thrust calculations of a standard thrust-drag bookkeeping scheme.

Another noteworthy observation is that the rate at which thrust-induced drag changes with a change in gross thrust input is much lower for the TCT compared to its podded propulsors. This is likely due to the benefit of BLI. The total mass flow rate of the BLI configuration is also 15% higher than that of the non-BLI configuration, as shown in Table 3, due to the greater number of propulsive units. This allows the TCT to operate at a lower FPR, resulting in a higher adiabatic efficiency.

Table 4 provides a summary of the shaft power required by the propulsive units of each of the configurations. As expected, the podded propulsors of the CRM-TCT require less shaft power than those of the CRM. However, the TCT requires a similar quantity of mechanical power as that of one wing propulsor when accounting for electrical transmission losses. Nonetheless, the CRM-TCT yields a PSC of 4.1% relative to the CRM.

Table 2 Drag coefficients in counts for the CRM and CRM-TCT at power-off and on conditions.

Configuration	CRM			CRM-TCT		
Power setting	0	Trim	Δ	0	Trim	Δ
Podded propulsors	35.2	132.6	97.4	23.0	86.3	63.3
Airframe and TCT	248.1	248.1	0.0	263.7	327.6	63.9
Total	318.4	513.3	194.9	309.7	500.2	190.5

Table 3 Propulsion system characteristics for the CRM and CRM-TCT configurations.

Configuration	CRM	CRM-TCT	
Propulsor	Podded	Podded	TCT
FPR	1.48	1.48	1.26
η_a (%)	93.8	93.8	95.7
$\dot{m}$ (kg/s)	567.0	368.4	562.0
T_{t_0} (K)	248.1	248.1	247.6
Gross Thrust (kN)	100.2	65.1	65.1

Table 4 Shaft power in Megawatts required by the CRM and CRM-TCT configurations at their trim conditions.

Configuration	CRM	CRM-TCT
Podded propulsors	17.8	11.5
TCT	-	11.0
Total	35.5	34.1

B. The Transonic Truss-Braced Wing

As with the CRM and the CRM-TCT, the aiframe's of the TTBW and TTBW-TCT are first trimmed with respect to angle of attack, α, to achieve the design cruise lift coefficient of 0.60. This results in a trimmed angle of attack of $\alpha = 2.20°$ for both configurations. Again, note that this does not include contributions from the free-air propulsors and all propulsion systems are turned off. The TTBW and TTBW-TCT are then trimmed in streamwise force by varying gross thrust input, iterating steady-state CFD solutions, and performing a linear interpolation. This is shown in Fig. 5, where the TTBW is trimmed with a gross thrust input of 26.0 kN for each of the wing propulsors, and the TTBW-TCT is trimmed with gross thrust inputs of 14.4 kN per propulsion unit.

Table 5 presents a breakdown of drag contributions for each configuration with power-on and power-off settings. As with the CRM and CRM-TCT, the differences in thrust share between the podded propulsors of the TTBW and TTBW-TCT results in a higher thrust-induced drag for the former. Similar trends can be observed when comparing the power-on drag values against those of the power-off cases. Table 6 lists some of the propulsion system flow quantities, which highlight the higher adiabatic efficiency of the TTBW-TCT's propulsion units. As with the CRM-TCT, this is likely due to the TTBW-TCT's higher total mass flow rate, which reduces the FPR required to satisfy the thrust-drag trim condition. Compared to the CRM-TCT, however, the TTBW-TCT has a 17% higher mass flow rate relative to the TTBW, leading to a greater benefit in PSC as shown in Table 7. Accounting for electrical transmission losses, the TTBW-TCT has a PSC of 5.9% relative to the TTBW configuration.

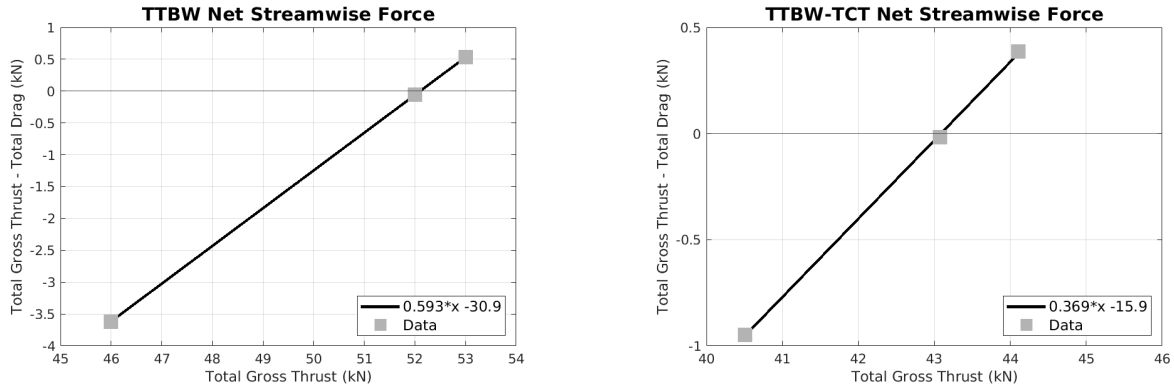

(a) TTBW **(b) TTBW-TCT**

Fig. 5 Net streamwise force versus total gross thrust input for the TTBW and TTBW-TCT configurations.

Table 5 Drag coefficients in counts for the TTBW and TTBW-TCT at power-off and on conditions.

Configuration	TTBW			TTBW-TCT		
Power setting	0	Trim	Δ	0	Trim	Δ
Podded propulsors	12.1	117.1	105.0	8.1	66.8	58.7
Airframe and TCT	254.4	254.4	0.0	260.8	271.0	10.2
Total	278.6	488.6	209.9	277.0	404.6	127.6

Table 6 Propulsion system characteristics for the TTBW and TTBW-TCT configurations.

Configuration	TTBW	TTBW-TCT	
Propulsor	Podded	Podded	TCT
FPR	1.41	1.33	1.28
η_a (%)	94.4	95.1	95.5
$\dot{m}$ (kg/s)	160.0	101.5	171.7
T_{t_0} (K)	244.5	244.5	244.4
Gross Thrust (kN)	26.0	14.4	14.4

Table 7 Shaft power in Megawatts required by the TTBW and TTBW-TCT configurations at their trim conditions.

Configuration	TTBW	TTBW-TCT
Podded propulsors	4.29	2.24
TCT	-	3.60
Total	8.58	8.08

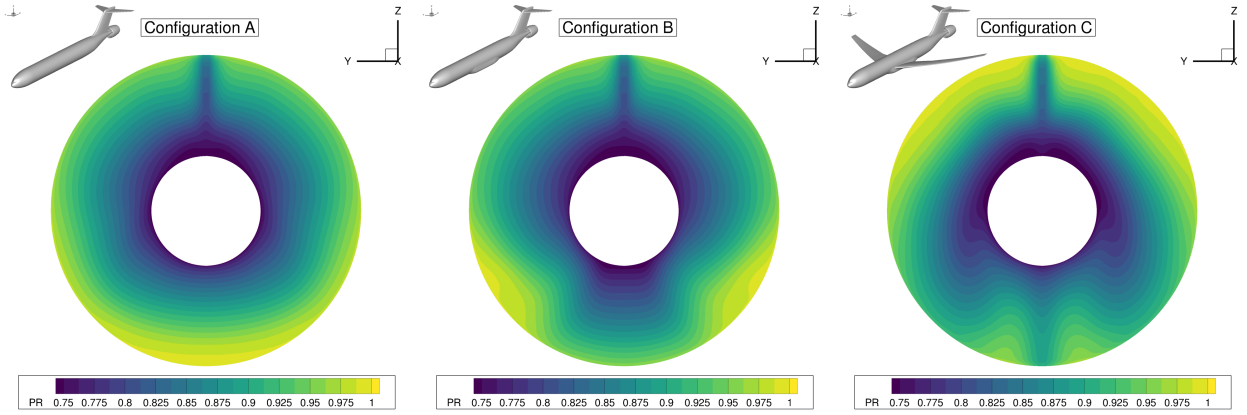

Fig. 6 Total pressure ratio contours at the nacelle highlight for the CRM-TCT.

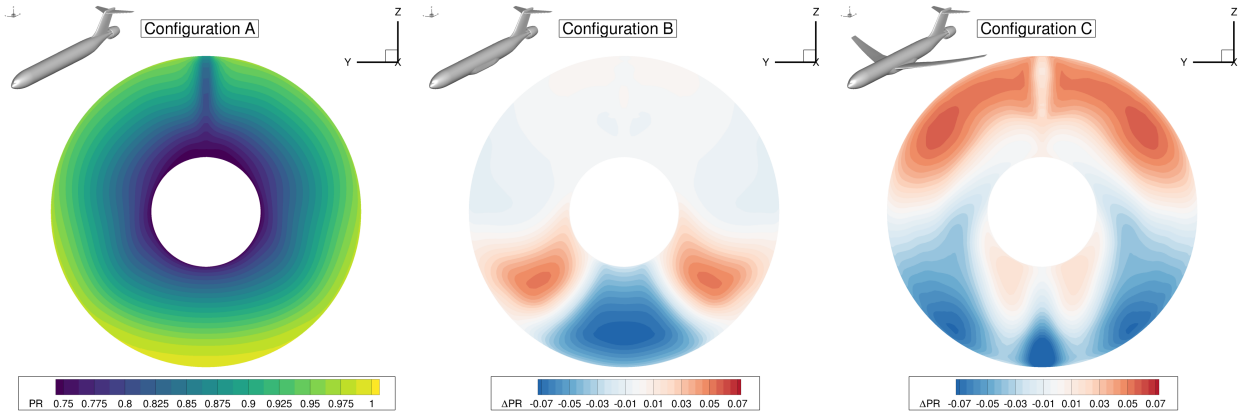

Fig. 7 Total pressure ratio difference with respect to Configuration A at the nacelle highlight for the CRM-TCT.

VI. Investigations of Inlet Distortion

As noted in Section I, inlet flow distortion poses significant challenges to the performance and operation of the fan. In order to examine the behavior of the flow at the nacelle inlet and identify the main contributors to the distortion profiles, component-by-component sensitivity studies are performed for the CRM-TCT and TTBW-TCT configurations. This involves a systematic approach in which airframe components are progressively added to the computational domain starting from a geometry with the fuselage, horizontal and vertical tails, and TCT only, and simulated at the trim condition with aeropropulsive analysis.

Figures 6 and 9 show total pressure contours at the nacelle highlight for the CRM-TCT and TTBW-TCT, respectively, which help to characterize inlet distortion [51, 52]. Specifically, total pressure ratio, or inlet total pressure recovery, is shown, which is given by

$$\mathrm{PR} = \frac{p_\mathrm{t}}{p_{\mathrm{t}_\infty}} \tag{7}$$

where p_t is the total pressure at the inlet and p_{t_∞} is the freestream total pressure. For reference, Figs. 7 and 10 show the total pressure ratio difference contours of each configuration with respect to the fuselage-tail-TCT case.

From the overall inlet distortion profiles of the CRM-TCT and TTBW-TCT configurations, namely, from Configuration C of Fig. 6 and Configuration D of Fig. 9, it can be seen that the flow patterns are remarkably similar, despite differences in wing configuration and aircraft class. These flow patterns consist of radially stratified low total pressure contours, whose core is formed by boundary layer flow from the fuselage, as highlighted in Configuration A of Figs. 6 and 9. This is typical for TCT propulsion system configurations, where the asymmetry is due to the upsweep of the fuselage tail section. The vertical region of low total pressure comes from the vertical tail.

In Configuration B of Fig. 6 and Configuration C of Fig. 9, it can be seen that the wing-fuselage fairings introduce two lobed regions in the total pressure contours near the bottom of the nacelle highlights. This appears to be due to

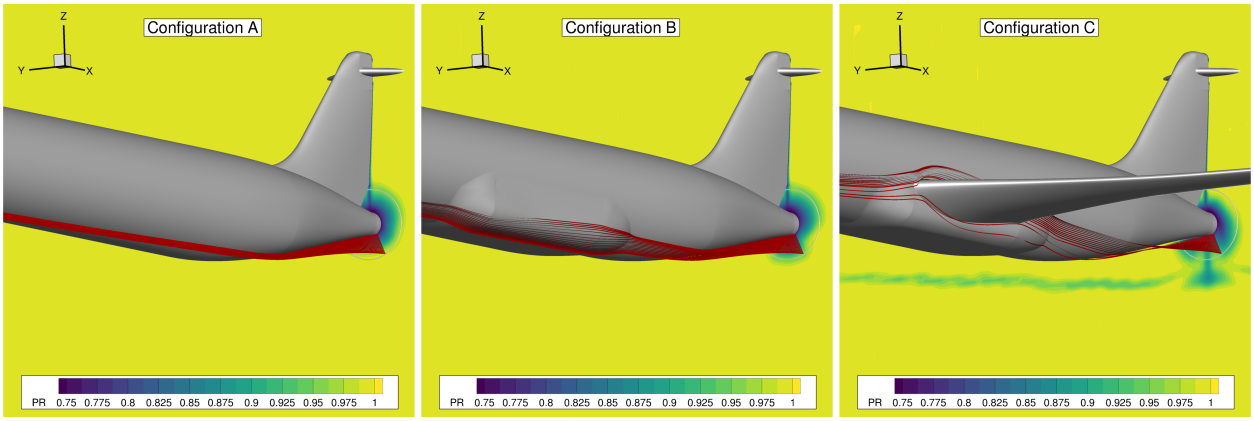

Fig. 8 Velocity streamlines highlighting the aft fuselage vortex structures for the CRM-TCT.

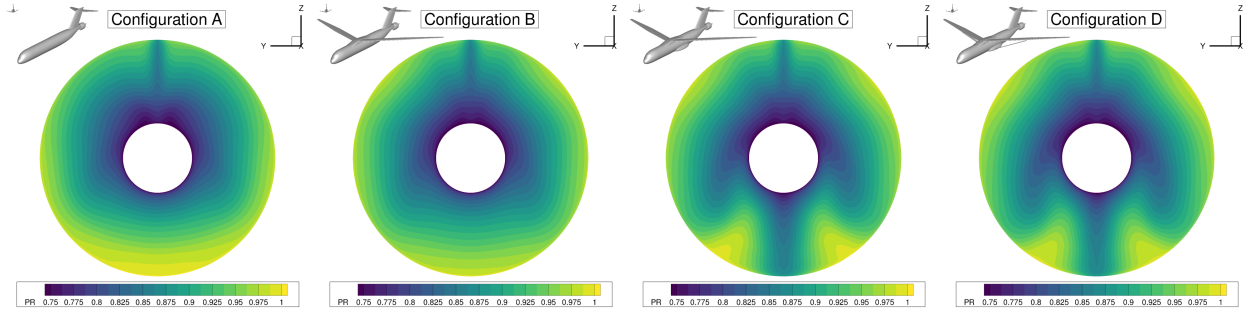

Fig. 9 Total pressure ratio contours at the nacelle highlight for the TTBW-TCT.

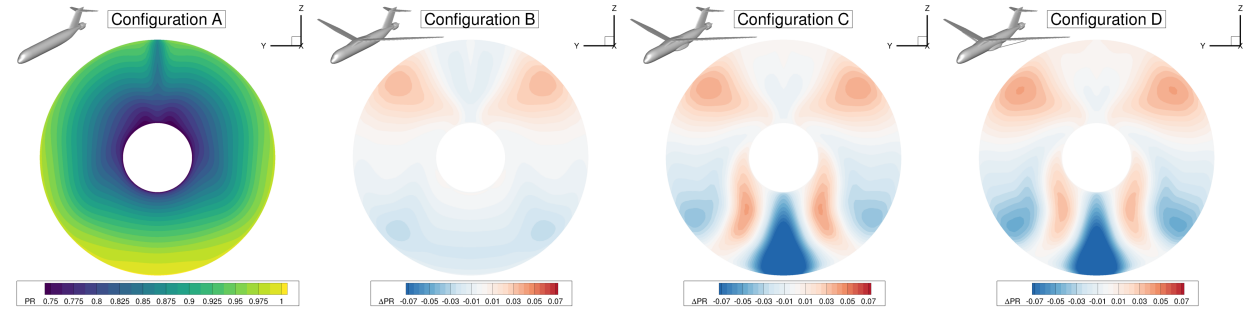

Fig. 10 Total pressure ratio difference with respect to Configuration A at the nacelle highlight for the TTBW-TCT.

vortex structures generated mainly from the fairing, as highlighted in Fig. 8 and 11. In Configuration C of Fig. 6 and Configuration D of Fig. 9, these lobed patterns are amplified, likely due to the downwash introduced by the wings. For the TTBW-TCT, however, it should be noted that the strut geometry does not contribute much to the total distortion pattern, even though it produces a small fraction of the total lift.

Another observation is that wing position significantly influences the distortion pattern. Fig. 7 shows that the low-wing configuration of the CRM-TCT has a much larger impact on the resulting distortion profile when compared to the high-wing configuration of the TTBW-TCT shown in Fig. 10. The low-wing configuration appears to generate stronger vortex structures, which impact the bottom portion of the inlet distortion profile, while the high-wing configuration results in a slightly more pronounced influence over the upper portion of the contours.

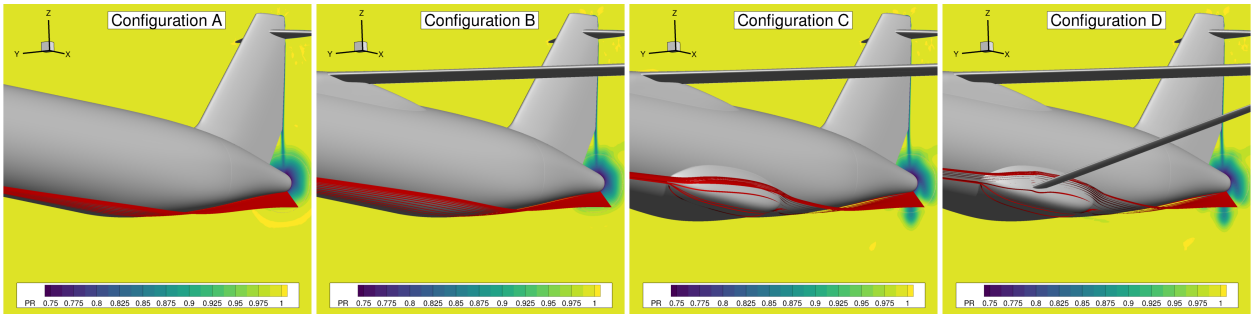

Fig. 11 Velocity streamlines highlighting the aft fuselage vortex structures for the TTBW-TCT.

VII. Conclusions

Given concerns over the environmental sustainability of the aviation industry, advanced aircraft technologies are sought to reduce aircraft fuel burn and emissions, and to improve their overall energy efficiency. One promising technology is the BLI TCT propulsion system, which can be applied to transport category aircraft with conventional fuselage configurations. Through the ingestion of low-momentum boundary layer flow developed over the airframe, aircraft configurations utilizing this technology can benefit from reduced shaft power requirements and hence improved aircraft efficiency.

In the present paper, the BLI TCT propulsion system technology enabled by an electrified powertrain is investigated for two different aircraft configurations: (1) a wide-body conventional tube-and-wing aircraft configuration based on the NASA CRM, and (2) a NASA-developed single-aisle TTBW configuration. The former is based on a model developed for testing in the NTF wind tunnel and establishes the approach used for assessing potential benefits, while the latter provides insight into the combination of two next-generation aircraft technologies that are of interest to the aviation sector.

Results indicate a PSC of 4.1% and 5.9% for the CRM-TCT and TTBW-TCT, respectively, when compared to their non-BLI counterparts. This assumes an end-to-end transmission efficiency of 90% for the BLI configurations. It is important to note, however, that the propulsion systems of all configurations were sized based on first principles, and not subjected to high-fidelity aeropropulsive optimization, which would improve the credibility of these estimates. For example, Gray et al. [15–17] and Yildirim et al. [18] optimized the shape of podded propulsors for minimum shaft power while subjecting them to constant thrust constraints. Nonetheless, these estimates are considered reasonable to first order, capturing the primary interactions between airframe aerodynamics and propulsion system performance, and highlighting the potential benefits of the technology.

Furthermore, as an additional next step in this study, it would be of interest to include the podded propulsors along with the airframe simulations. This would help capture the potential benefits of reducing interference effects between the podded propulsors and the wing, leveraging the smaller propulsor size achieved with the BLI configuration.

Component-by-component sensitivity studies were also performed for the two aircraft configurations to investigate the impact of their airframe components on the inlet distortion profiles. Results show that despite differences between the two aircraft configurations, most notably differences in their wing topology and wing position, the two inlet distortion patterns are remarkably similar. More specifically, the wing fairing of the CRM-TCT and strut fairing of the TTBW-TCT appear to play an important role in shaping the vortex structures generated toward the lower side of the up-swept fuselage tail section. The inlet distortion profiles also showed sensitivity to wing position, with the low-wing configuration of the CRM largely affecting the observed distortion profile relative to the high-wing configuration of the TTBW, which resulted in a less pronounced influence.

Future work will include high-fidelity gradient-based aeropropulsive shape optimization [53] to improve the credibility of the PSC estimates while incorporating considerations toward inlet flow distortion [17, 21]. Focus is also set on increasing the fidelity level of the actuator zone models by including efficiency losses within the model, moving toward a tighter coupling between the aerodynamics and propulsion models.

Acknowledgments

This work was supported by the Advanced Air Transport Technology (AATT) project under NASA's Aeronautics Mission Directorate (ARMD) Advanced Air Vehicles Program (AAVP). The authors would like to express their sincere

gratitude to Jeffrey Housman, Gerrit Stich, and the rest of the LAVA team for insightful input and feedback. Special appreciation is extended to Shishir Pandya for his guidance and leadership on this project, and review of this paper. The authors also acknowledge Mark Turner, Matthew Ha, and the rest of the BLITS team for valuable discussions. The authors would also like to thank Joshua Anibal and Brandon Lowe for internal review. Finally, the authors are also grateful to Gaetan Kenway for his assistance in setting up the Power Savings Coefficient calculation within LAVA. Computational resources were provided by the NASA High-End Computing Capability (HECC) Program through the NASA Advanced Supercomputing (NAS) Division at Ames Research Center.

References

[1] Hall, D., Huang, A., Uranga, A., Greitzer, E., Drela, M., and Sato, S., "Boundary Layer Ingestion Propulsion Benefit for Transport Aircraft," *Journal of Propulsion and Power*, Vol. 33, No. 5, 2017, pp. 1118–1129. https://doi.org/10.2514/1.B36321.

[2] Smith, A. M. O., and Roberts, H. E., "The Jet Airplane Utilizing Boundary Layer Air for Propulsion," *Journal of the Aeronautical Sciences*, Vol. 14, No. 2, 1947, pp. 97–109. https://doi.org/10.2514/8.1273.

[3] Drela, M., "Development of the D8 Transport Configuration," *29th AIAA Applied Aerodynamics Conference*, Honolulu, HI, 2012. https://doi.org/10.2514/6.2011-3970.

[4] Kawai, R., Friedman, D., and Serrano, L., "Blended Wing Body (BWB) Boundary Layer Ingestion (BLI) Inlet Configuration and System Studies," Tech. rep., NASA, December 2006.

[5] Liebeck, R., "Design of the Blended Wing Body Subsonic Transport," Vol. 41, 2004, pp. 10–25. https://doi.org/10.2514/1.9084.

[6] Hall, C. A., and Crichton, D., "Engine Design Studies for a Silent Aircraft," *Journal of Turbomachinery*, Vol. 129, No. 3, July 2006, pp. 479–487. https://doi.org/10.1115/1.2472398.

[7] Welstead, J., and Felder, J., "Conceptual Design of a Single-Aisle Turboelectric Commercial Transport with Fuselage Boundary Leyer Ingestion," *54th AIAA Aerospace Sciences Meeting*, San Diego, CA, 2016. https://doi.org/10.2514/6.2016-1027.

[8] Kim, H. D., Felder, J., Tong, M., and Armstrong, M., "Revolutionary Aeropropulsion Concept for Suitanable Aviation: Turboelectric Distributed Propulsion," *21st International Symposium on Air Breathing Engines (ISABE)*, Busan, Korea, 2013.

[9] Jansen, R. H., Kiris, C. C., Chau, T., Kenway, G. K. W., Machado, L. G., Duensing, J. C., Mirhashemi, A., Haglage, J. M., Dever, T. P., Chapman, J. W., French, B. D., Goodnight, T. W., Miller, L. R., Litt, J. S., Denham, C. L., Lynde, M., Campbell, R., Hiller, B., and Heersema, N., "Subsonic Single Aft Engine (SUSAN) Transport Aircraft Concept and Trade Space Exploration," *AIAA SciTech Forum*, AIAA 2022-2179, San Diego, CA, January 2022. https://doi.org/10.2514/6.2022-2179.

[10] Chau, T., and Duensing, J. C., "Conceptual Design of the Hybrid-Electric Subsonic Single Aft Engine (SUSAN) Electrofan Transport Aircraft," *AIAA SciTech Forum*, AIAA 2024-1326, Orlando, FL, January 2024. https://doi.org/10.2514/6.2024-1326.

[11] Schmollgruber, P., Döll, C., Hermetz, J., Liaboeuf, R., Ridel, M., Atinault, I. C. O., François, C., and Paluch, B., "Multidisciplinary Design and Performance of the ONERA Hybrid Electric Distributed Propulsion Concept (DRAGON)," *AIAA SciTech Forum*, AIAA 2020-0501, San Diego, CA, January 2019. https://doi.org/10.2514/6.2019-1585.

[12] Celestina, M. L., and Long-Davis, M. J., "Large-scale Boundary Layer Ingesting Propulsor Research," *International Society for Air Breathing Engines (ISABE) Conference*, ISABE, Canberra, Australia, September 2019.

[13] Rodriguez, D., "Multidisciplinary optimization method for designing boundary-layer-ingesting inlets," *Journal of Aircraft*, Vol. 46, No. 3, 2009, pp. 883–894. https://doi.org/10.2514/1.38755.

[14] Gray, J. S., Mader, C. A., Kenway, G. K., and Martins, J. R. R. A., "Approach to Modeling Boundary Layer Ingestion using a Fully Coupled Propulsion-RANS Model," *AIAA Scitech Forum*, Grapevine, Texas, January 2017. https://doi.org/10.2514/6.2017-1753.

[15] Gray, J. S., Mader, C. A., Kenway, G. K. W., and Martins, J. R. R. A., "Modeling Boundary Layer Ingestion Using a Coupled Aeropropulsive Analysis," *Journal of Aircraft*, Vol. 55, No. 3, 2018, pp. 1191–1199. https://doi.org/10.2514/1.C034601.

[16] Gray, J. S., and Martins, J. R. R. A., "Coupled Aeropropulsive Design Optimisation of a Boundary-Layer Ingestion Propulsor," *The Aeronautical Journal*, Vol. 123, No. 1259, 2019, pp. 121–137. https://doi.org/10.1017/aer.2018.120.

[17] Gray, J. S., Mader, C. A., Kenway, G. K. W., and Martins, J. R. R. A., "Coupled Aeropropulsive Optimization of a Three-Dimensional Boundary-Layer Ingestion Propulsor Considering Inlet Distortion," *Journal of Aircraft*, Vol. 57, No. 6, 2020, pp. 1014–1025. https://doi.org/10.2514/1.C035845.

[18] Yildirim, A., Gray, J. S., Mader, C. A., and Martins, J. R. R. A., "Boundary-Layer Ingestion Benefit for the STARC-ABL Concept," *Journal of Aircraft*, Vol. 59, No. 4, 2022, pp. 896–911. https://doi.org/10.2514/1.C036103.

[19] Hall, D. K., and Lieu, M., "Propulsor Models for Computational Analysis of Aircraft Aerodynamic Performance with Boundary Layer Ingestion," *AIAA Scitech Forum*, Virtual event, January 2021. https://doi.org/10.2514/6.2021-0991.

[20] Ordaz, I., Rallabhandi, S. K., Nielsen, E. J., and Diskin, B., "Mitigation of Engine Inlet Distortion through Adjoint-Based Design," *35th AIAA Applied Aerodynamics Conference*, Denver, CO, 2017, p. 3410. https://doi.org/10.2514/6.2017-3410.

[21] Kenway, G. K., and Kiris, C. C., "Aerodynamic shape optimization of the STARC-ABL concept for minimal inlet distortion," *2018 AIAA/ASCE/AHS/ASC Structures, Structural Dynamics, and Materials Conference*, 2018. https://doi.org/10.2514/6.2018-1912.

[22] Hirt, S. M., Arend, D. J., Wolter, J. D., and Johnson, A. M., "Development of a Flow Field for Testing a Boundary-Layer-Ingesting Propulsor," *53rd AIAA/SAE/ASEE Joint Propulsion Conference*, Atlanta, GA, 2017, p. 5043. https://doi.org/10.2514/6.2017-5043.

[23] Arend, D. J., Wolter, J. D., Hirt, S. M., Provenza, A., Gazzaniga, J. A., Cousins, W. T., Hardin, L. W., and Sharma, O., "Experimental Evaluation of an Embedded Boundary Layer Ingesting Propulsor for Highly Efficient Subsonic Cruise Aircraft," *53rd AIAA/SAE/ASEE Joint Propulsion Conference*, Atlanta, GA, 2017, p. 5041. https://doi.org/10.2514/6.2017-5041.

[24] Hardin, L. W., Cousins, W. T., Wolter, J. D., Arend, D. J., and Hirt, S. M., "Data Analysis Techniques for Fan Performance in Highly-Distorted Flows from Boundary Layer Ingesting Inlets," *2018 AIAA Aerospace Sciences Meeting*, Kissimmee, Florida, 2018, p. 1888. https://doi.org/10.2514/6.2018-1888.

[25] Provenza, A. J., Duffy, K. P., and Bakhle, M. A., "Aeromechanical Response of a Distortion-Tolerant Boundary Layer Ingesting Fan," *Journal of Engineering for Gas Turbines and Power*, Vol. 141, No. 1, 2018, 011011. https://doi.org/10.1115/1.4040739.

[26] Vassberg, J., Dehaan, M., Rivers, M., and Wahls, R., "Development of a Common Research Model for Applied CFD Validation Studies," *26th AIAA Applied Aerodynamics Conference*, Honolulu, HI, 2008, p. 6919. https://doi.org/10.2514/6.2008-6919.

[27] Chan, D. T., Jones, G. S., Langston, S. L., and Kwok, A. K., "Experimental Investigation of a Boundary Layer Ingesting Tailcone Thruster Configuration at the National Transonic Facility," *AIAA Aviation Forum*, AIAA 2024, Las Vegas, NV, July 2024.

[28] Fernandes, L. S., Machado, L. G., Duensing, J. C., and Kiris, C. C., "Computational Aerodynamics Analysis in Support of the CRM Tail Cone Thruster Configuration Wind Tunnel Test," *AIAA SciTech Forum*, AIAA 2022-1171, San Diego, CA, January 2022. https://doi.org/10.2514/6.2022-1171.

[29] Fernandes, L., Machado, L., Housman, J., and Duensing, J., "Computational Analysis of a Boundary-Layer Ingesting Tailcone Thruster Configuration within the National Transonic Facility using the LAVA Solver," *AIAA AVIATION 2024 Forum*, AIAA, Las Vegas, NV, 2024.

[30] Smith, L., "Wake Ingestion Propulsion Benefit," *Journal of Propulsion and Power*, Vol. 9, No. 1, February 1993, pp. 74–82. https://doi.org/10.2514/3.11487.

[31] Betz, A., *Introduction to the Theory of Flow Machines*, Pergamon Press, Oxford, England, UK, 1966.

[32] Drela, M., "Power Balance in Aerodynamic Flows," *AIAA Journal*, Vol. 47, No. 7, 2009, pp. 1761–1771. https://doi.org/10.2514/1.42409.

[33] Gray, J., "Design Optimization of a Boundary Layer Ingestion Propulsor Using a Coupled Aeropropulsive Model," Ph.D. thesis, University of Michigan, 2018.

[34] Greitzer, E. M., Bonnefoy, P., De la Rosa Blanco, E., Dorbian, C., Drela, M., Hall, D., Hansman, R., Hileman, J., Liebeck, R., Lovegren, J., et al., "Subsonic Ultra Green Aircraft Research: Phase I Final Report," Tech. rep., NASA, December 2010. NASA CR 2010-216794.

[35] Bradley, M., and Droney, C., "Subsonic Ultra Green Aircraft Research: Phase I Final Report," Tech. rep., NASA, April 2011. NASA CR 2011-216847.

[36] Scalabrin, L., and Felix, R., "Grid Assessment Using the NASA Common Research Model (CRM) Wind Tunnel Data," *51st AIAA Aerospace Sciences Meeting including the New Horizons Forum and Aerospace Exposition*, Grapevine, TX, 2013, p. 52. https://doi.org/10.2514/6.2013-52.

[37] Konig, B., and Fares, E., "Validation of a Transonic Lattice-Boltzmann Method on the NASA Common Research Model," *54th AIAA Aerospace Sciences Meeting*, San Diego, CA, 2016, p. 2023. https://doi.org/10.2514/6.2016-2023.

[38] Makino, S., Misaka, T., Kojima, T., Obayashi, S., and Sasaki, D., "Aerodynamic Analysis of NASA Common Research Model by Block-Structured Cartesian Mesh," *2018 AIAA Aerospace Sciences Meeting*, Kissimmee, Florida, 2018, p. 543. https://doi.org/10.2514/6.2018-0543.

[39] Chau, T., and Zingg, D. W., "Aerodynamic Design Optimization of a Transonic Strut-Braced-Wing Regional Aircraft," *Journal of Aircraft*, Vol. 59, No. 1, 2022, pp. 253–271. https://doi.org/10.2514/1.C036389.

[40] Chau, T., and Zingg, D. W., "Aerodynamic Optimization and Fuel Burn Evaluation of a Transonic Strut-Braced-Wing Single-Aisle Aircraft," *Journal of Aircraft*, Vol. 60, No. 5, 2023, pp. 1638–1658. https://doi.org/10.2514/1.C037158.

[41] Bradley, M. K., Droney, C. K., and Allen, T. J., "Subsonic Ultra Green Aircraft Research: Phase II - Volume I - Truss Braced Wing Design Exploration," Tech. rep., Boeing Research and Technology, April 2015. NASA/CR-2015-218704/Volume I.

[42] Kiris, C. C., Housman, J. A., Barad, M. F., Brehm, C., Sozer, E., and Moini-Yekta, S., "Computational Framework for Launch, Ascent, and Vehicle Aerodynamics (LAVA)," *Aerospace Science and Technology*, Vol. 55, No. 1, 2016, pp. 189–219. https://doi.org/10.1016/j.ast.2016.05.008.

[43] Housman, J. A., Kiris, C. C., and Hafez, M. M., "Time-Derivative Preconditioning Methods for Multicomponent Flows - Part I: Riemann Problems," *Journal of Applied Mechanics*, Vol. 76, No. 2, 2009, pp. 1–13. https://doi.org/10.1115/1.3072905.

[44] Housman, J. A., Kiris, C. C., and Hafez, M. M., "Time-Derivative Preconditioning Methods for Multicomponent Flows—Part II: Two-Dimensional Applications," *Journal of Applied Mechanics*, Vol. 76, No. 3, 2009, pp. 1–12. https://doi.org/10.1115/1.3086592.

[45] Spalart, P. R., and Allmaras, S. R., "A One-Equation Turbulence Model for Aerodynamic Flows," *30th AIAA Aerospace Sciences Meeting and Exhibit*, AIAA 92-0439, Reno, Nevada, January 1992. https://doi.org/10.2514/6.1992-439.

[46] Shur, M. L., Strelets, M. K., Travin, A. K., and Spalart, P. R., "Turbulence Modeling in Rotating and Curved Channels: Assessing the Spalart-Shur Correction," *AIAA Journal*, Vol. 38, No. 5, 2000, pp. 784–792. https://doi.org/10.2514/2.1058.

[47] Spalart, P. R., "Strategies for Turbulence Modelling and Simulations," *International Journal of Heat and Fluid Flow*, Vol. 21, No. 3, 2000, pp. 252–263. https://doi.org/10.1016/S0142-727X(00)00007-2.

[48] Saad, Y., and Schultz, M., "GMRES: A Generalized Minimal Residual Algorithm for Solving Nonsymmetric Linear Systems," 1986, pp. 856–869. https://doi.org/10.1137/0907058.

[49] Stich, G.-D., Fernandes, L. S., Duensing, J. C., Housman, J. A., Kenway, G. K. W., and Kiris, C. C., "Validation of Actuator Disk, Actuator Line and Sliding Mesh Methods within the LAVA Solver," *International Conference on Computational Fluid Dynamics 11*, ICCFD, Maui, HI, July 2022.

[50] Tinoco, E. N., Brodersen, O. P., Keye, S., Laflin, K. R., Feltrop, E., Vassberg, J. C., Mani, M., Rider, B., Wahls, R. A., Morrison, J. H., Hue, D., Roy, C. J., Mavriplis, D. J., and Murayama, M., "Summary Data from the Sixth AIAA CFD Drag Prediction Workshop: CRM Cases," *Journal of Aircraft*, Vol. 55, No. 4, 2018, pp. 1352–1379. https://doi.org/10.2514/1.C034409.

[51] Longley, J., and Greitzer, E., "Inlet Distortion Effects in Aircraft Propulsion System Integration," *Steady and transient performance prediction of gas turbine engines*, AGARD Lecture Series, Vol. 183, Advisory Group for Aerospace Research and Development (AGARD), Neuilly su Seine, France, 1992.

[52] *Inlet Total-Pressure-Distortion Considerations for Gas-Turbine Engines*, Aerospace Information Report 1419 (AIR1419), Revision D, SAE International, August 2023.

[53] Lowe, B. M., Ashby, C. P., Koch, J. R. L., Penner, D. A. C., Housman, J. A., and Duensing, J. C., "Towards Aerodynamic Shape Optimization Using an Immersed Boundary Overset Grid Method," *AIAA AVIATION 2024 Forum*, AIAA, Las Vegas, NV, 2024.